Modeling Hydrogen Evolution Reaction Kinetics through Explicit Water−Metal Interfaces

Michael T. Tang,[⊥] Xinyan Liu,[⊥] Yongfei Ji, Jens K. Norskov, and Karen Chan*

ABSTRACT: Despite the apparent simplicity of the hydrogen evolution reaction (HER) and the decades of research into it, controversy remains in the literature regarding the identity of the active site and the competition between the Heyrovsky and Tafel steps. In this work, we use charge-extrapolated ab initio simulations with explicit water in conjunction with mean-field microkinetic modeling to explore the mechanism for HER on both close-packed (111) and stepped (211) transition metals. First, we show that atop H*, beyond a monolayer of hollow H*, is unlikely to play a role in the HER mechanism, given its very positive adsorption energies. The energetics suggests the Volmer−Heyrovsky mechanism to predominate on fcc transition metals under typical operating conditions. We evaluate our theoretical results vs several experimental observations. We show that the Volmer−Heyrovsky mechanism predicts an activity volcano with its peak at a H* binding $\Delta G_{H^*} \approx 0$ eV, consistent with experiment. In contrast, the Volmer−Tafel volcano shows a broad rate plateau between $\Delta G_{H^*} \approx 0$ eV and $\Delta G_{H^*} \approx -0.4$ eV. We find our theoretical Tafel slopes to be consistent with experimental ones on a range of transition metals. We show that, in line with experimental observations, the introduction of a CO(g) atmosphere shifts the strong binding metals toward the weak binding leg. Our study suggests that the simple thermodynamic approach to HER activity still holds, even when a detailed kinetic picture is considered.

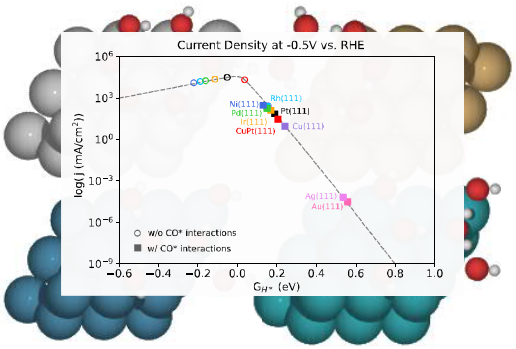

1. INTRODUCTION

Sustainable hydrogen-based energy storage systems[1,2] necessitate a mechanistic understanding of electrochemical hydrogen evolution reaction (HER).

Hydrogen evolution involves three elementary reactions:

(i)

$$H^+ + e^- \leftrightarrow H^* \quad \text{Volmer step}$$

(ii)

$$H^+ + e^- \leftrightarrow H^* \quad \text{Heyrovsky step}$$

(iii)

$$H^* + H^* \leftrightarrow H_2 \quad \text{Tafel step}$$

Despite the apparent simplicity of the reaction and decades of research, controversy remains in the literature regarding the role of overpotential (OPD) vs underpotential deposited (UPD) H* and the competition between the Heyrovsky and Tafel steps.[3−15]

Existing models typically examine the Tafel slopes of HER to determine the rate-limiting step of HER.[3,4,6,7,11,13,14,16−24] A Tafel slope of around 30 mV/dec is commonly reported in acidic HER on Pt by many groups,[17,19,20,25] consistent with the Volmer−Tafel route; however, it has been shown by several authors that this 30 mV/dec slope corresponds to a fully diffusion limited current density.[21,26] When diffusion limitations are mitigated with H_2-pump experiments or with microelectrodes,[7,14,23] a Tafel slope of 120 mV/dec on Pt is reported.[21] The ongoing debate on Tafel slope measurements pertains to the mechanistic studies, where some studies suggest Pt(110) to be Tafel-limited,[3,9] whereas Pt(100) is reported as Heyrovsky-limited.[10] It remains unclear whether HER is dominated by a Volmer−Heyrovsky or a Volmer−Tafel mechanism and whether the predominant mechanism shifts with transition metal surfaces.

Another controversy in the HER literature pertains to the active adsorbate species in H_2 formation. UPD (underpotential deposited) H* corresponds to H* adsorbed above the H_2 equilibrium potential ($U > 0$ V vs RHE) and OPD (overpotential deposited) H* to those adsorbed below.[17,25,27−31] On strong binding metals such as Pt, these

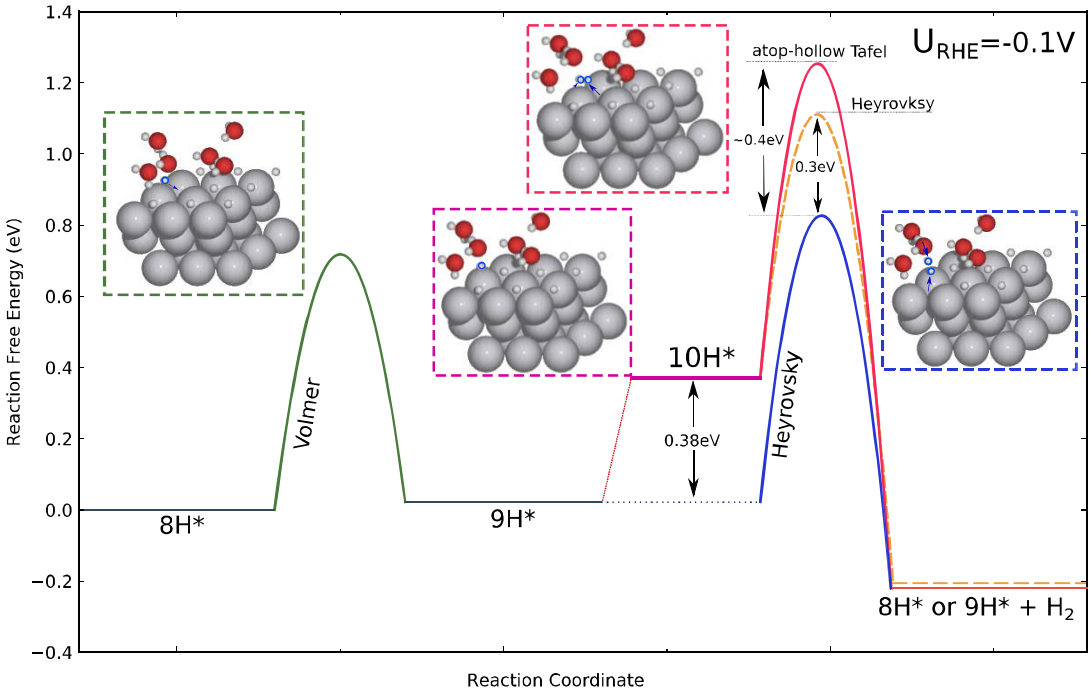

Figure 1. Free-energy diagram of Pt(111) at U_{RHE} = −0.1 V, showing Volmer−Tafel and Volmer−Heyrovsky routes around 1 ML H* (θ_{H^*} = 0.88−1.11 ML). The insets show images of transition states, with blue circles and arrows indicating the proton or hydrogen of interest. The transition state of the Volmer step shows a proton moving toward an atop site before setting in a hollow site. The transition state of a Heyrovsky step on a 1 ML covered surface shows a hollow H* moving toward an atop site as it associates with the incoming proton. The Tafel state shows association of the 10th atop-bound H* with a nearby hollow-bound H*.

species have been assigned to different sites;[27] the usual assumption is that UPD H* is more coordinated (adsorbed on hollow sites[32]) and more strongly bound than OPD H* (adsorbed on atop sites[5,33,34]). The significance of this distinction between the UPD and OPD H* is that it suggests UPD H* to be a spectator species, whereas the OPD H* adsorb on atop sites above 1 monolayer (ML) of UPD H* and are active for HER. Despite intensive research efforts, the question regarding the nature of the active H* species remains debated in the recent literature.[35,36]

In this work, we use ab initio simulations with explicit water, in conjunction with mean-field microkinetic modeling, to investigate trends in the HER mechanism on both close-packed fcc(111) and stepped fcc(211) transition metals. Our computational analysis elucidates the controversies mentioned above. First, we show that it is unlikely that we exceed 1 ML of H* coverage under HER conditions, even on the strong binding metals. Next, we present a kinetic HER volcano built with kinetic scaling relations via metal surfaces across different H* coverages, considering both the Volmer−Heyrovsky and Volmer−Tafel as viable routes. We find the Heyrovsky step to be slightly more facile than the Tafel step. Moreover, we find that only the Volmer−Heyrovsky mechanism gives a $\Delta G_{H^*} \approx 0$ eV volcano peak, consistent with experimental trends. Our kinetic model is furthermore consistent with the potential dependence of experimental Tafel slopes on Ag, Au, and Pt, as well as with the experimentally observed shifts in HER activity in a CO atmosphere. Most importantly, our study suggests that the simple thermodynamic picture of HER activity still holds, where $\Delta G_{H^*} \approx 0$ eV gives the optimal activity.

2. METHODS

2.1. DFT Calculations. Reaction energetics were calculated with density functional theory with a periodic plane-wave implementation and ultrasoft pseudopotentials using the QUANTUM ESPRESSO code,[37] interfaced with the atomistic simulation environment (ASE).[38] We applied the BEEF-vdW functional, which provides a reasonable description of van der Waals forces while maintaining an accurate prediction of chemisorption energies.[39] Plane-wave and density cutoffs were 500 and 5000 eV, respectively, with a Fermi-level smearing width of 0.1 eV. A Monkhorst−Pack k-point grids of [4 × 4 × 1] was employed.[40] Thermochemical H* binding energies were determined on six-layer transition metal slabs to reduce uncertainty from slab energetic convergence. Electrochemical barriers were calculated within (3 × 3) supercells on fcc(111) surfaces and (3 × 1) ones on fcc(211) surfaces, with at least three atomic layers where atoms in the top layer are relaxed and the rest are fixed, along with a hydrogen-bonded water layer. Transition state geometries and energies were calculated using the climbing-image nudged elastic band (CI-NEB) method, with the forces on the climbing image converged to less than 0.05 eV $Å^{-1}$. The spring constants were tightened for images close to the saddle point. The charge extrapolation method[42] was used to deduce the transition states at constant potential (details below). All transition states were referenced to the initial state of aqueous protons and electrons in bulk solution,[41] as determined using the reversible/computational hydrogen electrode. For electrochemical barriers, we shift H-down water structures around the surface and selecting the lowest transition state energy. Tafel barriers were calculated with similar supercells without water layers. All energetics plotted in free-energy diagrams and scaling relations are

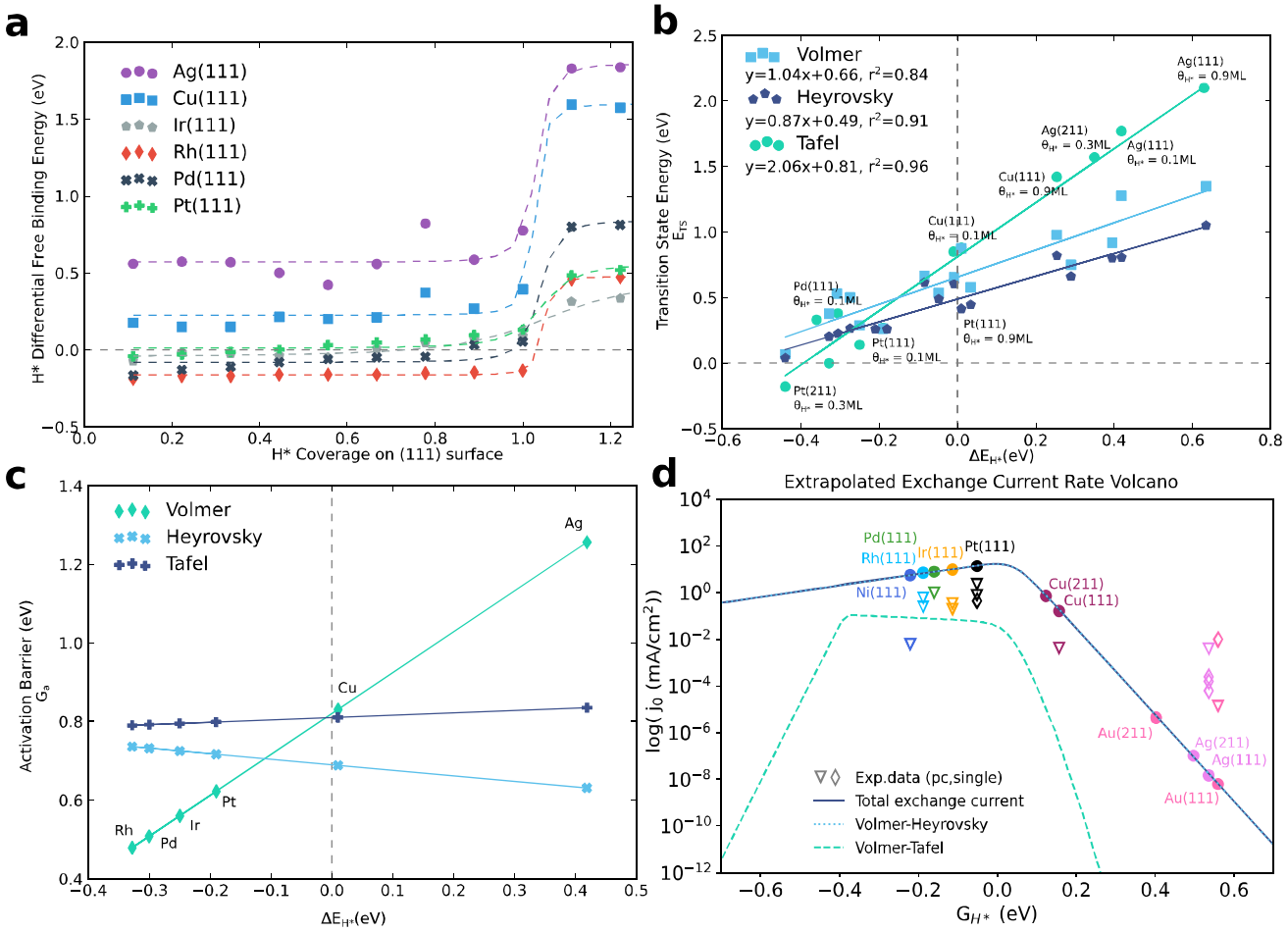

Figure 2. (a) Differential H* free binding energy on transition−metal fcc(111) surfaces as a function of H* surface coverage up to the first two atop H* on a fully H* covered surface. To guide the eye, the figure uses a fitted algebraic equation parameterized with the form $\frac{x}{\sqrt{1+x^2}}$ to fit the free binding energies on all metals up until the second atop H* past 1 ML coverage (H* cov: 1.22 ML). (b) Scaling relations of the charge-extrapolated Volmer, Heyrovsky, and Tafel transition state energies vs H* binding energy. Certain points are labeled, the rest can be found in Tables S1 and S2. (c) Barriers vs H* binding energies. (d) Extrapolated exchange current densities as a function of G_{H^*}. Experimental points are taken from ref 48.

referenced to H_2 gas and bulk protons in solution (or the clean metal state).[41] Scaling relations were derived from "unscaled transition state energy" (calculated and charge-extrapolated transition state energy from NEB calculations); the transition state data across the metal surfaces considered in this study are provided in Tables S1 and S2. We then use linear scaling equations to determine "scaled transition state energies" based on the H* binding energy of a given metal surface, and our kinetics are computed from these scaling relations.

Steady-state, mean-field microkinetic models were simulated with the CATMAP software package.[43] All relaxed structures and energetics are available on the Catalysis-Hub database: https://www.catalysis-hub.org/publications/TangModeling2020.[44]

2.2. The Charge Extrapolation Scheme. The absolute potential at the interface was determined by the work function relative to vacuum and referenced to the experimental work function of the standard hydrogen electrode, 4.4 eV.[45] GGA-level functionals can lead to incorrect band alignment of solvent and water, which leads to artificial charge transfer at the interface. This problem is mitigated with the usage of counterions, a shift in water structure, or the application of a Hubbard U.[46] In this work, we have applied H-down water structures, which present the least issues with band alignment for negatively charged slabs. Close to the potential of zero charge (0.3 V vs SHE), the net orientation of waters is close to neutral.[11] We therefore assume that the strong dipole from H-down water adds an artificial contribution to the potential obtained from the work function. The net dipole from the H-down water orientation was found to be approximately 1.3 eV, and this value was subtracted from the calculated work function to correct for the effect of using an artificially H-down oriented water layer in the simulations.

3. RESULTS AND DISCUSSION

3.1. On the Nature of H* Species under HER. We examined the differential H* adsorption energies on Ag(111), Cu(111), Pt(111), Ir(111), Pd(111), and Rh(111). We find that the hollow site are clearly preferred on weak binding metals such as Ag and Cu as well as strong binding metals, Pd and Rh. (On Pd, we have left out the possibility of hydride formation.) For Pt and Ir, we find atop sites to be 0.1 eV more stable than the hollow sites, though such a difference is within

the uncertainty in DFT calculations.[47] For simplicity, we assume that the hollow sites are occupied first on all metals.

In the literature on Pt-like metals, OPD H* has been suggested to correspond to atop sites and is kinetically distinct from the UPD H* assumed to occupy hollow sites.[27,32] This leads to the suggestion that the H* fill up hollow sites as a spectator species, and that only H* bound on atop sites above 1 ML H* are active.[25,27,35] To investigate this assumption, we show in Figure 1 the competition between a Heyrovsky step on a hollow H* (at 1 ML H*) vs both Tafel and Heyrovsky steps off an atop H* at >1 ML H*. We have included images of transition states as well as an image of 10 H* adsorbed on the 3 × 3 Pt(111) cell corresponding to $\theta_{H^*} = 1.11$ (the barriers they correspond to are indicated by the color of their borders). Given the differential binding energetics in Figure 2a, Pt(111) has a saturation coverage of around 0.66 ML at 0 V vs RHE. We therefore consider an applied potential of $U_{RHE} = -0.1$ V to obtain $\theta_{H^*} = 1$ on Pt(111) so that we can evaluate the kinetic contributions of hollow H* vs the atop H* that is adsorbed above 1 ML H*.

The free energies in Figure 1 start with eight hollow H* on Pt(111) (in a 3 × 3 cell such that $\theta_{H^*} = 0.8$). The ninth hollow H* is adsorbed through a Volmer step to give a $\theta_{H^*} = 1$; we find that the transferring proton tends to approach the top site as it adsorbs onto the hollow ones. H_2 can be evolved from these hollow H* through a Heyrovsky step (blue) or a Tafel one (not shown). In this Heyrovsky step, we find that the H* migrates toward the top site en route to meet with the incoming proton.

To evaluate the hypothesis that hydrogen evolution occurs with atop H* at $\theta_{H^*} > 1$, we consider the two pathways for H_2 evolution from the 10th H* (in the 3 × 3 cell, this corresponds to $\theta_{H^*} = 1.11$ ML). To keep the figure simple, we have omitted the corresponding Volmer barrier (which we calculated to be 0.69 eV at −0.1 V) to adsorb this 10th H*. Note that the adsorption free energy of the 10th atop H* is $\Delta G_{H^*} = 0.48$ eV at $U_{RHE} = 0$ V (see Figure S12 for energetics). This process thus becomes exergonic only at $U_{RHE} = -0.48$ V, well beyond the onset for HER in acid. At $U_{RHE} = -0.1$ V shown in Figure 1, $\Delta G_{H^*} = 0.38$ eV and the corresponding Boltzmann coverage of these atop species is $\theta_{H^*_{top}} = 10^{-6}$. The Heyrovsky and atop-hollow Tafel barriers off this 10th H* are shown in orange dashed line and red solid line, respectively.

We estimate the differences in TOF between the different pathways at −0.1 V vs RHE using the Boltzmann coverages and the computed barriers. Assuming a prefactor A of 10^{13}, the TOF for a Tafel step associated with H^*_{fcc} and a H^*_{top} at $\theta_{H^*} > 1$ is

$$r_{taf-top} = A\theta_{H^*_{top}}\theta_{H^*_{fcc}}\exp\left(-\frac{E_a}{k_B T}\right) = A \times 10^{-6} \times 1 \exp\left(-\frac{0.86\ \text{eV}}{k_B T}\right) = \sim 10^{-8}/\text{s} \quad (1)$$

Similarly, the Heyrovsky step associated with a H^*_{top} with a $\theta_{H^*_{top}} = 10^{-9}$ at over 1 ML H* has a barrier of 0.7 eV with a corresponding TOF of

$$r_{hey-top} = A \times 10^{-6} \times \exp\left(-\frac{0.7\ \text{eV}}{k_B T}\right) = \sim 10^{-5}/\text{s} \quad (2)$$

In contrast, the TOF associated with a Heyrovsky step off a H* at or just below 1 ML H* (assumed to be in hollow, fcc sites) is orders of magnitude higher:

$$r_{hey-fcc} = A \times 1 \times \exp\left(-\frac{0.77\ \text{eV}}{k_B T}\right) = \sim 1/\text{s} \quad (3)$$

From these estimates of TOF, the activity off the Heyrovsky from the H* adsorbed at or below 1 ML surface coverage are far from spectators and dominate the activity.

Our calculations on Pt(111) do not definitively show that H* adsorbs initially on hollow sites since they differ in stability from the atop sites by only 0.1 eV. We have therefore included consideration of the 10th H* over a fully atop-covered surface and found a 0.1 eV difference in its binding energy compared to the fully hollow-covered surface, as shown in Figure S12. So the idea that the H* species adsorbed below 1 ML is much more active for HER still holds even if the top sites were occupied first. We also note that infrared reflection−absorption spectroscopy (IRAS) has been applied as an attempt to identify the reaction intermediate for HER. These studies have reproducibly measured a very weak vibration at ∼2090 cm^{-1} on both polycrystalline and single-crystal Pt surfaces,[17,33,34] suggesting the presence of atop H*. However, this result does not indicate the existence of significant atop H* above 1 ML, nor does it suggest which H* species is most active for HER.

In summary, we expect the H* coverage on Pt(111) to saturate at around $\theta_{H^*} = 1$. Coverages of H* species above a monolayer are orders of magnitude smaller and contribute negligibly to HER activity. We find no inactive H* species deposited only above the equilibrium potential (UPD conditions) that is distinct from active H* species that is deposited only below (OPD conditions). Additionally, Figure 2a illustrates that, across transition metals considered in this study, H* in atop sites at $\theta_{H^*} > 1$ ML always possess a significantly higher adsorption energy. Once the H* coverage reaches 1 ML, subsequent H* adsorption is thermodynamically unfavorable for all metals under typical potentials for HER.

3.2. Universal fcc(111) and fcc(211) Kinetic Scaling.

Next, we examine the universal transition-state scaling of the HER elementary steps. Figure 2b shows the scaling relations for the transition state energies of the Volmer, Heyrovsky, and Tafel steps on fcc(111) surfaces at $\theta_{H^*} = 0.11$ as well as on fcc(211) surfaces at $\theta_{H^*} = 0.88$. The Volmer and Heyrovsky transition states correspond to a potential of $U = 0$ V vs RHE (pH = 0), as determined from charge extrapolation. We note that, in this subplot, the transition state energy is referenced to the clean metal slab; the distinction between transition state energy, E_{TS}, and activation barrier, $E_a = E_{TS} - E_{IS}$, is shown in Figure S13. Activation free-energy barriers, $G_a = G_{TS} - G_{IS}$, are determined via harmonic approximation using the vibrational modes found in Table S5. Thus, while Pt(211) has a somewhat negative Tafel E_{TS}, the corresponding G_a is positive because the 2H* initial state is far more negative. Figure 2b allows one to see how the transition state energies shifts with changes to H* binding energy; tuning the H* binding energy more positive (less stable) in turn shifts the transition state energies higher.

Figure 2c shows the corresponding activation barriers at 0 V vs RHE (pH = 0) for the three steps. These barriers are derived from taking the linear fitted E_{TS} from the scaling relations in Figure 2b, then referencing them to the respective

initial states of the Volmer, Heyrovsky, and Tafel step such that $E_a = E_{TS} - E_{IS}$. The results are plotted and listed in Table S4. Figure 2c illustrates how the barriers change with H* binding energy, which in turn affects the rate volcano shape (discussed later). As expected, Volmer and Heyrovsky barriers have opposite slopes with respect to H* binding energy, with the Volmer step being less facile on weak binding metals and the reverse for the Heyrovsky step. The same figure shows the Tafel association barrier to have a very small slope with respect to H* binding energy, which suggests an initial state-like transition state. We see a 0.1−0.2 eV difference between the Heyrovsky and Tafel step at a potential of $U_{RHE} = 0$ V.

Figure 2d shows the exchange current density volcanoes vs H* free binding energy, determined from the transition state scaling relations and the corresponding barriers in Figure 2b,c. The exchange current densities were determined through linear extrapolation from the current densities at $U = -0.1$ V to $U = -0.3$ V vs RHE, where the Tafel approximation to the Butler−Volmer equation is valid. The exchange rate of the volcano is within 1−2 orders of magnitude agreement with the experimentally measured exchange current densities on Pt-like metals.[9,45,48] The largest discrepancy between experiments and the calculated exchange rate is regarding Ag and Au on the Volmer leg; however, the discrepancy may be due to possible defect sites not considered in this study.

In addition to the overall exchange rate, Figure 2d also shows the decomposition of the volcano into the Volmer−Tafel and Volmer−Heyrovsky contributions. Strikingly, there is a flat plateau spanning a 0.4 eV range in G_{H^*} at the top of the Volmer−Tafel volcano, which is not observed in experiments regarding tuning the H* binding energy using metallic alloys.[49,50] The flat plateau of the Volmer−Tafel volcano is attributed to the weak correlation between the Tafel activation barrier vs the hydrogen binding energy shown in Figure 2c. Figure S13d shows that the 2H* state and the H−H transition state correlate nearly one-to-one, suggesting that the H−H state stabilizes by a similar amount as the 2H* state for the transition metals considered in this study.

In terms of partial rates, the Volmer−Heyrovsky mechanism dominates for all metals considered, while Volmer−Tafel volcano shows around 1−2 orders of magnitude smaller contribution to the overall rate. The relative order of magnitude of the Heyrovsky vs Tafel rates is dependent on the particular potential reference applied in calculating barriers. However, the flat region of the Volmer−Tafel volcano remains regardless of the potential referencing scheme, which suggests a Volmer−Heyrovsky mechanism to dominate on all transition metals considered. We note that the leftmost leg on the Volmer−Tafel volcano corresponds to a region where G_{H^*} is so negative that the transition state energy of the Tafel step drops below than the H_2 gas state (see Figure S1 for how the FED influences the activity volcano legs) such that its reaction rate is determined by the reaction energy. Finally, Figure S10 shows the evolution of the HER rate volcano with applied potential and how the charge transfer coefficient β of the Volmer and Heyrovsky step may change the shape of the rate volcano.

3.3. Tafel Slopes. Table 1 shows the experimental Tafel slopes reported by the literature compared with slopes determined by the microkinetic model. We have classified the reported values into two bins: one determined from the activity at small overpotentials $U_{applied} \geq -0.1$ V and one determined from the activity at higher overpotentials $U_{applied} < -0.1$ V. Some works report two Tafel slopes corresponding approximately to these two regions. We note that it is generally not meaningful to consider the ones in the small overpotential region. By definition, a Tafel slope is only defined where the Tafel approximation to the Butler−Volmer equation is valid, e.g., where the cathodic branch dominates at potentials negative enough of equilibrium. At small overpotentials ($U_{applied} \geq -0.1$ V), there are contributions from both forward and backward reactions such that log j does not vary linearly with voltage.[55] For completeness, however, we have included them in the table though they cannot really be called "Tafel slopes". In general, for the three metals considered, we find simulated Tafel slopes of close to −120 mV/dec for all metals considered at overpotentials < -0.1 V, consistent with literature reports. We furthermore note that, on Pt, Tafel slopes around[17,19,20,25] −30 mV/dec slope can arise from diffusion limitations;[13,21,26] when transport limitations are mitigated through H_2-pump experiments or with micro-electrodes,[7,14,23] a −120 mV/dec slope is also recovered.

Table 1. Comparison of Experimentally Reported vs Theoretical Tafel Slopes in Different Overpotential Regimes[a]

metal surface	experimental "Tafel slopes" $U_{applied} \geq -0.1$ V	experimental Tafel slopes $U_{applied} \geq -0.1$ V	theoretical Tafel slopes $U_{applied} \geq -0.1$ V
Pt	−37*[3,11], −30,[17] −30[20,21]	74#,[3] 112#,[3] 120†[21,25]	−121
Ag	−59,[51] −60[16]	112[16]	−118
Au	−65,[52] −50*[31], −68[53]	−114,[52] −123,[54] −105*,[31] −120[53]	−118

[a]Slopes are reported in units of mV/dec. We take experimental Tafel slopes from both polycrystalline electrodes and single-crystal electrodes (the (111) data are labeled with an asterisk (*). (100) Data from ref 3 labeled with a pound sign (#) may have not considered solution resistance and can be heavily diffusion limited). Data labeled with a dagger (†) are determined through fit through the BV equation. Theoretical Tafel slopes were calculated for the Pt(111), Ag(211), and Au(211) facets. We also note that for the low overpotentials $U_{applied} \geq -0.1$ V, a Tafel approximation to the Butler−Volmer equation is not valid, but we include the reported slopes for completeness. Theoretical Tafel slopes are determined in the Tafel regime where $U_{applied} < -0.1$ V.

Figure 3a shows the Tafel plots on Pt(111), Ag(211), and Au(211) using the scaling relations formed from Figure 2b. The Tafel slopes can be rationalized for both the weak binding (right leg) and strong binding (left leg) metals. In the weak binding case, $\theta_H \rightarrow 0$ (see coverage plots for Ag(211) and Au(211) in Figure S8). With a Volmer−Heyrovsky mechanism, the corresponding rate is then

$$R = A a_{H^+} \exp\left(-\frac{G_a^{Volmer} + e\beta U_{SHE}}{k_B T}\right) \quad (4)$$

where a_{H^+} is the activity of protons in solution, and G_a^{Volmer} is the Volmer activation barrier. A $\beta = 0.5$ results in a Tafel slope of around 120 mV/dec. On strong binding metals like Pt(111), $\theta_H \rightarrow 1$ (see coverage plot in Figure S8). The corresponding rate is therefore given by

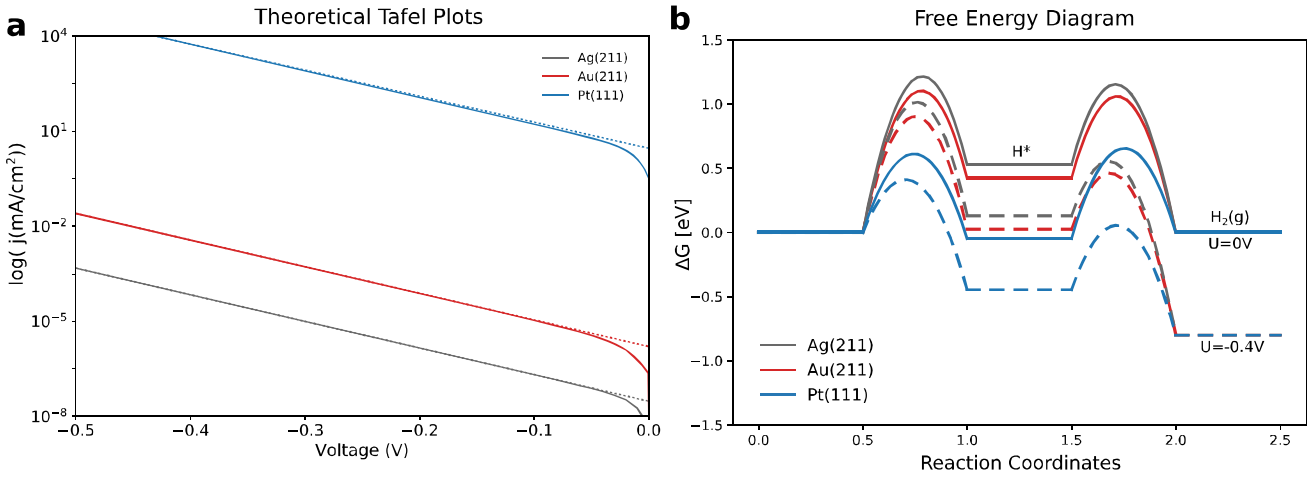

Figure 3. (a) Tafel plot of Pt(111), Ag(211), and Au(211). Where the Tafel approximation to the Butler−Volmer equation is valid ($U_{applied} < -0.1$ V), we find a Tafel slope of near −120 mV/dec on all three metals. (b) Free-energy diagram of Pt(111), Ag(211), and Au(211) from applied potentials $U = 0$ to −0.4 V.

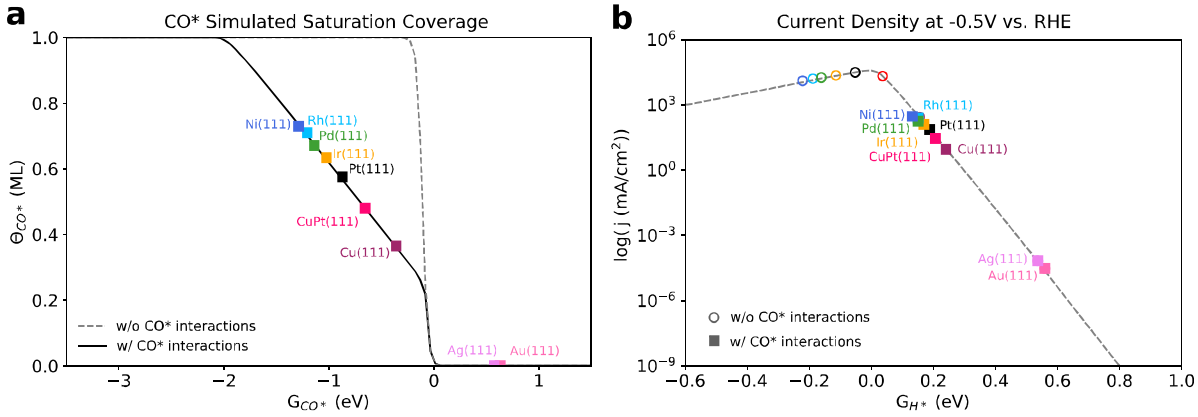

Figure 4. (a) Predicted CO* equilibrium coverage at −0.5 V vs RHE from the model with and without interactions. Solid squares denote predicted CO* coverage on the metal surface using an interacting model. (b) H_2 production current densities at −0.5 V vs RHE, in the presence and in the absence of CO(g). The differential H* binding free energy under the reaction condition is used as the x axis.

$$R = Aa_{H^+}\theta_{H^*}\exp\left(-\frac{G_a^{Heyrovsky} + e\beta U_{SHE}}{k_B T}\right) = Aa_{H^+}\exp\left(-\frac{G_a^{Heyrovsky} + e\beta U_{SHE}}{k_B T}\right) \quad (5)$$

which again results in a −120 mV/dec Tafel slope. Note here that the coverage of H* is saturated at unity once enough potential is applied.

Finally, Figure 3b shows the corresponding free-energy diagrams of Pt(111), Ag(211), and Au(211) as a function of potential. It is shown that, on Pt(111), the transition state for the Heyrovsky step Pt(111) decreases much faster than that for the Volmer barrier since it is the second proton−electron transfer step and therefore shifts with $(1+\beta)$ compared to the Volmer barrier (β).[55] However, the H* coverage ($\theta_{H^*} \approx 1$, as shown in Figure S8) also affects the activity, and so its overall rate can be determined by eq 5, which contains the Heyrovsky barrier. Similarly, the free-energy diagram of Ag(211) and Au(211) shows that the energies of the transition states for both Volmer and Heyrovsky steps are similar when no applied potential is applied. The weak H* binding on both metal surfaces means a small $\theta_{H^*} \approx 0$ (see Figure S8). The overall rate can thus be determined by the Volmer barrier, as in eq 4.

3.4. Note on Our Barriers vs Previous Studies.

Compared to previous studies on Pt(111),[35,56,57] we find that our Tafel barriers (0.77−0.83 eV) are within the ranges proposed by other DFT methods. Likewise, Skúlason et al.[9] report a Volmer barrier of 0.69 eV on Pt(111), whereas we measured a similar barrier of 0.61 eV. The most notable difference in our work are the Heyrovsky barriers (0.62−0.74 eV), which others have generally reported to be much higher (1.4 eV).[9,57] The difference may lie in the consideration of the energy difference between bulk and interface proton−electron pairs;[35,41] without referencing to bulk proton−electrons (see Figure S14 for further clarification), our Heyrovsky barriers near 1 ML would lie around 1.2 eV and our Volmer barriers around 0.57 eV. Nevertheless, we provide the microkinetics in a case where Heyrovsky has a 1.4 eV barrier as reported in these previous studies while keeping the Volmer and Tafel barriers the same as this work for Pt(111). The result is shown Figure S7. With such a high Heyrovsky barrier, the Tafel step limits the overall activity. Using a transfer coefficient of 0.5, the electrochemical Volmer barriers can decrease with applied potential; however, the Tafel barrier cannot. Thus, if Pt(111)

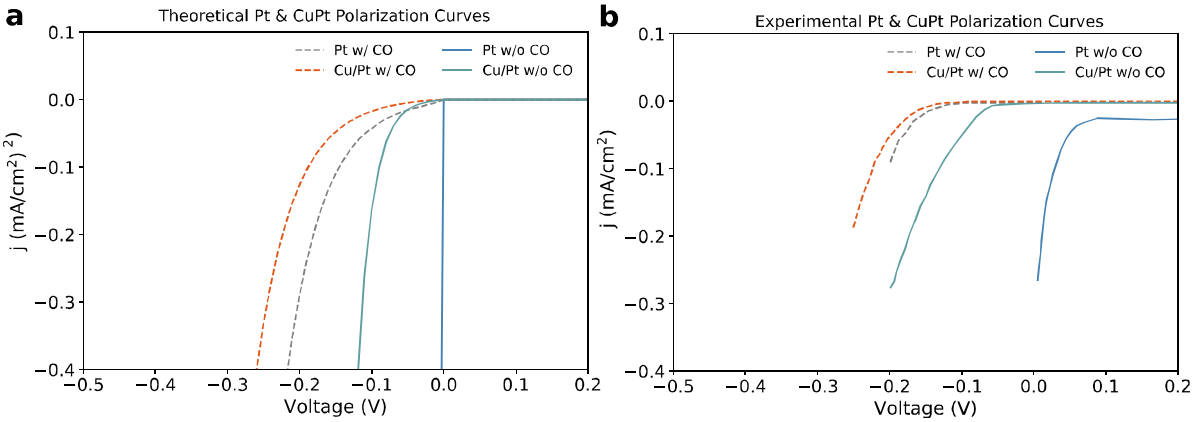

Figure 5. (a) Theoretically predicted and (b) experimentally measured polarization curves on Pt(111) and Cu overlayer on Pt(111) with and without CO(g). Polarization curves were simulated with assumptions that $\beta_{\text{Volmer}} = 0.5$, $\beta_{\text{Heyrovsky}} = 0.5$. Experimental curves are taken from refs 66, 67.

were to only run the Volmer–Tafel mechanism, a flat Tafel slope is obtained at potentials $U_{\text{RHE}} < -0.1$ V, in stark contrast to the −120 mV/dec slope given by the Volmer–Heyrovsky mechanism.

3.5. Note on Hydrogen Oxidation. As an aside, the inverse of the HER suggests a similar predominance of the Heyrovsky step; given the barriers in Figure S9, we find that a reverse Heyrovsky barrier is slightly more energetically favorable than the reverse Tafel step on most metals. Figure S6 shows that the Tafel slope in the HOR potential range ($U_{\text{RHE}} = 0.1$ V to $U_{\text{RHE}} = 0.3$ V) is −120 mV/dec, in agreement with Durst et al.[13] determined via the H_2 pump.

3.6. HER with the Presence of CO and OH. HER can occur in the presence of other adsorbates, for example, CO* under CO_2 reduction conditions, or *OH, which can be present on oxophilic metals under HER conditions. They adsorb as follows:

(i) $CO \leftrightarrow CO^*$

(ii) $H_2O \leftrightarrow OH^* + H^+ + e^-$

Thus, we consider the impact of *CO and *OH on HER. Figure S10 shows the differential adsorption energy of CO* on the Pt(111) surface as a function of coverage, where adsorption energy starts to monotonically increase beyond a coverage of 0.25 ML. We apply a first-order adsorbate–adsorbate interaction model[58] that is shown to provide a good description of the coverage-dependent adsorption energies metal surfaces; in the particular case in Figure S10, the error between the model (line) and DFT calculations (points) is typically less than 0.2 eV, similar to the uncertainty brought by DFT calculations.[47] Given the similarity in size between OH* and CO*, we treat OH* interactions to be identical to CO* interactions, where we apply a first-order interaction model with an onset threshold at 0.25 ML (see Figure S10), interaction parameters are also included in Supplemental Note 6.

As shown in Figure 4a, the CO* coverage is predicted to saturate to 1 ML as soon as ΔG_{CO^*} binding energy is below 0.0 eV when no adsorbate–adsorbate interactions are introduced. This is in contrast with the model with adsorbate–adsorbate interactions, where an extra −2 eV in ΔG_{CO^*} binding energy is needed to reach 1 ML CO* coverage. The effect of interactions is therefore the most pronounced for the surfaces with moderate binding strength. For the weak binding surfaces such as Ag and Au, CO* coverages stay near 0 such that no observable CO* repulsive interaction takes place. Metals with strong CO* binding of around $\Delta G_{CO^*} < -1.5$ eV still lead to near 1 ML covered surfaces. On metals with moderate CO* binding strength (-1.5 eV $< \Delta G_{CO^*} < -0.5$ eV), the inclusion of interactions enables better predictions of saturation CO* coverage. For example, the saturation CO* coverage on Pt(111) is reported to be around 0.6 ML,[59−61] consistent with the microkinetic model with adsorbate–adsorbate interactions as shown in (a), whereas the non-interacting model grossly overestimates the CO* coverage to be 1 ML on Pt(111).

The adsorption of CO* on metal surfaces leave H* with weaker binding sites, which also in turn lead to a lower H* coverage on all metals. This is shown in the 2D coverage map in Figure S4, where even with an applied potential of $U_{\text{RHE}} = -0.5$ V, the CO* coverage hovers around 0.4–0.7 ML on Pt-like metals, while the H* coverage is shown to be effectively 0 for all metals considered. This suggests that CO* "blocks" H* from the remaining sites. In similar studies, sulfur has also been found to block active sites on Pt(111), leading to a notable decrease in HER activity when θ_{S^*} goes from 0 to 0.3 ML.[62,63]

Figure 4b depicts the hydrogen evolution activity volcano under −0.5 V vs RHE, with and without the presence of CO. The hollow points are metals with their H* binding energies in the low H* coverage regime, whereas the solid points are predicted H* binding energy under the CO sparged environment. Under the CO environment, metals with moderate to strong CO binding energies are shifted toward the Volmer leg of the activity volcano due to the weakened H* binding in the presence of *CO.[59,64] The metals shift along the transition state scaling relations in Figure 2b such that the activation barriers increase in accordance to the weakened H* binding energy; the resultant activity volcano with the presence of CO remains similar to the one without. This is in agreement with the work done by Jaramillo et al.[64] and Peterson et al.[65] using a thermodynamic analysis. Interestingly, very strong H* binding surfaces like Ni may possess a sufficiently facile Volmer barrier despite the introduction of adsorbed CO*, which result in a reversal of the activity trends in CO-free environments.

Metals with strong OH* binding energy will likely retain a small OH* coverage at the onset potential of HER. Figure S3a depicts a 2D coverage map of OH* on (111) metal surfaces at −0.1 V vs RHE under acidic (pH = 0) HER conditions. For most transition metals, OH* binding energies are too positive

to adsorb any OH* under HER conditions. However, CuPt(111), where a monolayer of Cu is layered over Pt(111),[66] is found to adsorb OH* strongly on the oxophilic Cu monolayer surface. As a result, Figure S3b shows the effects of OH* poisoning on a 2D (E_{H^*}, E_{OH^*}) HER current density volcano, where there is a notable decrease in activity when a surface binds OH* strongly.

We have also simulated the polarization curves to investigate the effect on catalytic activities brought by CO* and OH*. Figure 5 exhibits the predicted polarization curves on Pt(111) and Cu/Pt(111), with and without CO, along with the experimental observations. As indicated by the blue solid line, HER on Pt takes off immediately after 0 V vs RHE in the absence of CO, exhibiting negligible overpotential. This is consistent with the fact that Pt is demonstrated by numerous studies to be ideal for HER and serves as a widely accepted catalyst benchmark.[9,13,30,31,64,67] As indicated by the gray dashed line in Figure 5, the addition of CO poisons the Pt surface and inhibits its HER activity. An overpotential of about 0.2 V is required to surmount such an effect. Within the Tafel regime and given the charge transfer coefficient $\beta = 0.5$, we observed a similar Tafel slope of −120 mV/dec between Pt(111) and Pt(111) with CO presence.

Similarly, there is also a suppression of HER on a Cu overlayer on Pt(111) (Cu/Pt(111)) in the presence of CO, as indicated by the orange dashed line, though the shift in onset is smaller than in the Pt(111) case. This effect arises from the presence of OH* on Cu/Pt(111) without CO*. In the presence of *CO, the adsorbate displaces *OH. Since both *OH and *CO suppress HER, the net result in a smaller shift in activity than in the Pt(111) case, upon switching from a CO-free to CO environment. Figure S5 shows the Tafel slope of CuPt with and without CO presence to be similar at late overpotentials. When OH* poisoning is present, there is an earlier Tafel slope of around −46 mV/dec according to our microkinetic model.

In both Cu/Pt(111) and Pt(111), the shift in overpotential is described by the theoretical model with reasonable accuracy. This resemblance between the theoretical predictions and experimental observations suggests the validity of using a first-order adsorbate−adsorbate interaction model to describe the impact of *CO and *OH under HER conditions.

4. CONCLUSIONS

In this work, we applied the charge extrapolation scheme to determine electrochemical barriers for the hydrogen evolution reaction. We uncover several trends that may aid the ongoing mechanistic debate regarding active species and rate-limiting steps of HER. On Pt(111), we find that the energetics for H* adsorption above 1 ML is very endergonic. Therefore, H* coverage converges toward 1 ML, and the same trends hold across a variety of transition metal surfaces considered.

Next, we have determined kinetic scaling relations of the Volmer and Heyrovsky steps for the (111) and (211) surfaces. We find universal scaling lines across the surfaces and H coverages considered. Overall, we find that our scaling lines produce an exchange current density volcano that corroborate with experimental results. We also find that only the Volmer−Heyrovsky route produces a volcano optimum at $\Delta G_{H^*} \approx 0$ eV, whereas the Volmer−Tafel route produces a rate plateau, which suggests the former mechanism to dominate on all transition metals considered.

Using mean-field microkinetic modeling, the corresponding Tafel slopes on Ag, Au, and Pt were also found to be consistent with experiment. Nevertheless, as our study simply models with a charge transfer coefficient $\beta = 0.5$, future studies should look into conditions where the charge transfer coefficient may deviate from the supposed 0.5 value. Additionally, we included CO* and OH* interactions into our microkinetic model to show the changes in HER rates due to the adsorption of other intermediates. The effectiveness of the interaction model is suggested by Pt(111) and Cu:Pt(111) polarization curves.

Finally, our work demonstrates that, even after a full kinetic treatment is considered, the H* binding energy remains a relevant descriptor for optimizing HER rates. Surfaces possessing significant quantities of sites with H* free binding energy close to zero produce the highest HER rates.

AUTHOR INFORMATION

Corresponding Author

Karen Chan − *CatTheory section, Department of Physics, Technical University of Denmark, Lyngby 2800, Denmark;* orcid.org/0000-0002-6897-1108; Email: kchan@fysik.dtu.dk

Authors

Michael T. Tang − *Department of Material Science and Engineering, Stanford University, Stanford, California 94305, United States; SUNCAT Center for Interface Science and Catalysis, SLAC National Accelerator Laboratory, Menlo Park, California 94025, United States;* orcid.org/0000-0002-7190-4723

Xinyan Liu − *SUNCAT Center for Interface Science and Catalysis, SLAC National Accelerator Laboratory, Menlo Park, California 94025, United States*

Yongfei Ji − *School of Chemistry and Chemical Engineering, Guangzhou University, Guangzhou 51006, China;* orcid.org/0000-0002-6759-7126

Jens K. Norskov − *CatTheory section, Department of Physics, Technical University of Denmark, Lyngby 2800, Denmark;* orcid.org/0000-0002-4427-7728

Complete contact information is available at:

Author Contributions

[⊥]M.T.T. and X.L. contributed equally.

Notes

The authors declare no competing financial interest.

■ ACKNOWLEDGMENTS

This project has been supported by the Joint Center for Artificial Photosynthesis (JCAP), a DOE Energy Innovation Hub, supported through the Office of Science of the U.S. Department of Energy under award no. DE-SC0004993. We acknowledge the use of computer time allocation at the National Energy Research Scientific Computing Center, a DOE Office of Science User Facility supported by the Office of Science of the U.S. Department of Energy under contract no. DE-AC02-05CH11231. M.T.T. and X.L. thank JCAP for financial support. J.K.N. and K.C. also acknowledge financial support from V-Sustain: The VILLUM Centre for the Science of Sustainable Fuels and Chemicals (#9455) from VILLUM FONDEN. Y.J. thanks the Knut & Alice Wallenberg Foundation for financial support through the "Wallenberg Postdoctoral Scholarship Program" at Stanford. Finally, we thank Dr. Hector Prats Garcia for discussions regarding experimentally measured HER kinetics.

■ REFERENCES

(1) Brynolf, S.; Taljegard, M.; Grahn, M.; Hansson, J. Electrofuels for the transport sector: A review of production costs. *Renewable Sustainable Energy Rev.* **2018**, *81*, 1887−1905.

(2) Züttel, A.; Remhof, A.; Borgschulte, A.; Friedrichs, O. Hydrogen: the future energy carrier. *Philos. Trans. R. Soc., A* **2010**, *368*, 3329−3342.

(3) Marković, N. M.; Grgur, B. N.; Ross, P. N. Temperature-Dependent Hydrogen Electrochemistry on Platinum Low-Index Single-Crystal Surfaces in Acid Solutions. *J. Phys. Chem. B* **1997**, *101*, 5405−5413.

(4) Conway, B. E.; Jerkiewicz, G. Relation of energies and coverages of underpotential and overpotential deposited H at Pt and other metals to the 'volcano curve' for cathodic H2 evolution kinetics. *Electrochim. Acta* **2000**, *45*, 4075−4083.

(5) Kunimatsu, K.; Senzaki, T.; Samjeské, G.; Tsushima, M.; Osawa, M. Hydrogen adsorption and hydrogen evolution reaction on a polycrystalline Pt electrode studied by surface-enhanced infrared absorption spectroscopy. *Electrochim. Acta* **2007**, *52*, 5715−5724.

(6) Barber, J.; Morin, S.; Conway, B. E. Specificity of the kinetics of H2 evolution to the structure of single-crystal Pt surfaces, and the relation between opd and upd H. *J. Electroanal. Chem.* **1998**, *446*, 125−138.

(7) Tavares, M. C.; Machado, S. A. S.; Mazo, L. H. Study of hydrogen evolution reaction in acid medium on Pt microelectrodes. *Electrochim. Acta* **2001**, *46*, 4359−4369.

(8) Rossmeisl, J.; Skúlason, E.; Björketun, M. E.; Tripkovic, V.; Nørskov, J. K. Modeling the electrified solid-liquid interface. *Chem. Phys. Lett.* **2008**, *466*, 68−71.

(9) Skúlason, E.; Tripkovic, V.; Björketun, M. E.; Gudmundsdóttir, S.; Karlberg, G.; Rossmeisl, J.; Bligaard, T.; Jónsson, H.; Nørskov, J. K. Modeling the Electrochemical Hydrogen Oxidation and Evolution Reactions on the Basis of Density Functional Theory Calculations. *J. Phys. Chem. C* **2010**, *114*, 18182−18197.

(10) Cai, Y.; Anderson, A. B. The Reversible Hydrogen Electrode: Potential-Dependent Activation Energies over Platinum from Quantum Theory. *J. Phys. Chem. B* **2004**, *108*, 9829−9833.

(11) Ledezma-Yanez, I.; Wallace, W. D. Z.; Sebastián-Pascual, P.; Climent, V.; Feliu, J. M.; Koper, M. T. M. Interfacial water reorganization as a pH-dependent descriptor of the hydrogen evolution rate on platinum electrodes. *Nat. Energy* **2017**, *2*, 17031.

(12) Strmcnik, D.; Tripkovic, D.; van der Vliet, D.; Stamenkovic, V.; Marković, N. M. Adsorption of hydrogen on Pt(111) and Pt(100) surfaces and its role in the HOR. *Electrochem. Commun.* **2008**, *10*, 1602−1605.

(13) Durst, J.; Simon, C.; Hasché, F.; Gasteiger, H. A. Hydrogen Oxidation and Evolution Reaction Kinetics on Carbon Supported Pt, Ir, Rh, and Pd Electrocatalysts in Acidic Media. *J. Electrochem. Soc.* **2014**, *162*, F190−F203.

(14) Durst, J.; Siebel, A.; Simon, C.; Hasché, F.; Herranz, J.; Gasteiger, H. A. New insights into the electrochemical hydrogen oxidation and evolution reaction mechanism. *Energy Environ. Sci.* **2014**, *7*, 2255−2260.

(15) Eberhardt, D.; Santos, E.; Schmickler, W. Hydrogen evolution on silver single crystal electrodes−first results. *J. Electroanal. Chem.* **1999**, *461*, 76−79.

(16) Antoniou, A. A.; Wetmore, F. E. W. Cathodic Polarization of Silver in Sulphuric Acid. *Can. J. Chem.* **1959**, *37*, 222−227.

(17) Kunimatsu, K.; Senzaki, T.; Tsushima, M.; Osawa, M. A combined surface-enhanced infrared and electrochemical kinetics study of hydrogen adsorption and evolution on a Pt electrode. *Chem. Phys. Lett.* **2005**, *401*, 451−454.

(18) Strmcnik, D.; Uchimura, M.; Wang, C.; Subbaraman, R.; Danilovic, N.; van der Vliet, D.; Paulikas, A. P.; Stamenkovic, V. R.; Markovic, N. M. Improving the hydrogen oxidation reaction rate by promotion of hydroxyl adsorption. *Nat. Chem.* **2013**, *5*, 300−306.

(19) Santana, J. A.; Mateo, J. J.; Ishikawa, Y. Electrochemical Hydrogen Oxidation on Pt(110): A Combined Direct Molecular Dynamics/Density Functional Theory Study. *J. Phys. Chem. C* **2010**, *114*, 4995−5002.

(20) Seto, K.; Iannelli, A.; Love, B.; Lipkowski, J. The influence of surface crystallography on the rate of hydrogen evolution at Pt electrodes. *J. Electroanal. Chem. Interfacial Electrochem.* **1987**, *226*, 351−360.

(21) Zheng, J.; Yan, Y.; Xu, B. Correcting the Hydrogen Diffusion Limitation in Rotating Disk Electrode Measurements of Hydrogen Evolution Reaction Kinetics. *J. Electrochem. Soc.* **2015**, *162*, F1470−F1481.

(22) Sheng, W.; Gasteiger, H. A.; Shao-Horn, Y. Hydrogen Oxidation and Evolution Reaction Kinetics on Platinum: Acid vs Alkaline Electrolytes. *J. Electrochem. Soc.* **2010**, *157*, B1529.

(23) Neyerlin, K. C.; Gu, W.; Jorne, J.; Gasteiger, H. A. Study of the Exchange Current Density for the Hydrogen Oxidation and Evolution Reactions. *J. Electrochem. Soc.* **2007**, *154*, B631.

(24) Markovića, N. M.; Sarraf, S. T.; Gasteiger, H. A.; Ross, P. N. Hydrogen electrochemistry on platinum low-index single-crystal surfaces in alkaline solution. *J. Chem. Soc.,Faraday Trans.* **1996**, *92*, 3719−3725.

(25) Conway, B. E.; Bai, L. Determination of adsorption of OPD H species in the cathodic hydrogen evolution reaction at Pt in relation to electrocatalysis. *J. Electroanal. Chem. Interfacial Electrochem.* **1986**, *198*, 149−175.

(26) Sheng, W.; Myint, M.; Chen, J. G.; Yan, Y. Correlating the hydrogen evolution reaction activity in alkaline electrolytes with the hydrogen binding energy on monometallic surfaces. *Energy Environ. Sci.* **2013**, *6*, 1509−1512.

(27) Conway, B. E.; Tilak, B. V. Interfacial processes involving electrocatalytic evolution and oxidation of H2, and the role of chemisorbed H. *Electrochim. Acta* **2002**, *47*, 3571−3594.

(28) Jerkiewicz, G.; Zolfaghari, A. Comparison of Hydrogen Electroadsorption from the Electrolyte with Hydrogen Adsorption from the Gas Phase. *J. Electrochem. Soc.* **1996**, *143*, 1240.

(29) Conway, B. E.; Bai, L. State of adsorption and coverage by overpotential-deposited H in the H2 evolution reaction at Au and Pt. *Electrochim. Acta* **1986**, *31*, 1013−1024.

(30) Marković, N. M.; Ross, P. N., Jr. Surface science studies of model fuel cell electrocatalysts. *Surf. Sci. Rep.* **2002**, *45*, 117−229.

(31) Kibler, L. A.; Hermann, J. M.; Abdelrahman, A.; El-Aziz, A. A.; Jacob, T. New insights on hydrogen evolution at Au single crystal electrodes. *Curr. Opin. Electrochem.* **2018**, *9*, 265−270.
(32) Zolfaghari, A.; Jerkiewicz, G. Temperature-dependent research on Pt(111) and Pt(100) electrodes in aqueous H2SO4. *J. Electroanal. Chem.* **1999**, *467*, 177−185.
(33) Bewick, A.; Russell, J. W. Structural investigation by infra-red spectroscopy of adsorbed hydrogen on platinum. *J. Electroanal. Chem. Interfacial Electrochem.* **1982**, *132*, 329−344.
(34) Nichols, R. J.; Bewick, A. Spectroscopic identification of the adsorbed intermediate in hydrogen evolution on platinum. *J. Electroanal. Chem. Interfacial Electrochem.* **1988**, *243*, 445−453.
(35) Lindgren, P.; Kastlunger, G.; Peterson, A. A. A Challenge to the G∼0 Interpretation of Hydrogen Evolution. *ACS Catal.* **2019**, *10*, 121−128.
(36) Exner, K. S. Does a Thermoneutral Electrocatalyst Correspond to the Apex of a Volcano Plot for a Simple Two-Electron Process? *Angew. Chem., Int. Ed.* **2020**, *59*, 10236−10240.
(37) Giannozzi, P.; Baroni, S.; Bonini, N.; Calandra, M.; Car, R.; Cavazzoni, C.; Ceresoli, D.; Chiarotti, G. L.; Cococcioni, M.; Dabo, I.; et al. QUANTUM ESPRESSO: a modular and open-source software project for quantum simulations of materials. *J. Phys.: Condens. Matter* **2009**, *21*, 395502.
(38) Larsen, A. H.; Mortensen, J. J.; Blomqvist, J.; Castelli, I. E.; Christensen, R.; Dułak, M.; Friis, J.; Groves, M. N.; Hammer, B.; Hargus, C.; et al. The atomic simulation environment−a Python library for working with atoms. *J. Phys.: Condens. Matter* **2017**, *29*, 273002.
(39) Wellendorff, J.; Silbaugh, T. L.; Garcia-Pintos, D.; Nørskov, J. K.; Bligaard, T.; Studt, F.; Campbell, C. T. A benchmark database for adsorption bond energies to transition metal surfaces and comparison to selected DFT functionals. *Surf. Sci.* **2015**, *640*, 36−44.
(40) Monkhorst, H. J.; Pack, J. D. Special points for Brillouin-zone integrations. *Phys. Rev. B* **1976**, *13*, 5188−5192.
(41) Chen, L. D.; Bajdich, M.; Martirez, J. M. P.; Krauter, C. M.; Gauthier, J. A.; Carter, E. A.; Luntz, A. C.; Chan, K.; Nørskov, J. K. Understanding the apparent fractional charge of protons in the aqueous electrochemical double layer. *Nat. Commun.* **2018**, *9*, 3202. , Number: 1 Publisher: Nature Publishing Group
(42) Chan, K.; Nørskov, J. K. Electrochemical Barriers Made Simple. *J. Phys. Chem. Lett.* **2015**, *6*, 2663−2668.
(43) Medford, A. J.; Shi, C.; Hoffmann, M. J.; Lausche, A. C.; Fitzgibbon, S. R.; Bligaard, T.; Nørskov, J. K. CatMAP: A Software Package for Descriptor-Based Microkinetic Mapping of Catalytic Trends. *Catal. Lett.* **2015**, *145*, 794−807.
(44) Winther, K. T.; Hoffmann, M. J.; Boes, J. R.; Mamun, O.; Bajdich, M.; Bligaard, T. Catalysis-Hub.org, an open electronic structure database for surface reactions. *Sci. Data* **2019**, *6*, 75.
(45) Trasatti, S. The absolute electrode potential: an explanatory note (Recommendations 1986). *Pure Appl. Chem.* **1986**, *58*, 955−966.
(46) Björketun, M. E.; Zeng, Z.; Ahmed, R.; Tripkovic, V.; Thygesen, K. S.; Rossmeisl, J. Avoiding pitfalls in the modeling of electrochemical interfaces. *Chem. Phys. Lett.* **2013**, *555*, 145−148.
(47) Medford, A. J.; Wellendorff, J.; Vojvodic, A.; Studt, F.; Abild-Pedersen, F.; Jacobsen, K. W.; Bligaard, T.; Nørskov, J. K. Assessing the reliability of calculated catalytic ammonia synthesis rates. *Science* **2014**, *345*, 197−200.
(48) Nørskov, J. K.; Bligaard, T.; Logadottir, A.; Kitchin, J. R.; Chen, J. G.; Pandelov, S.; Stimming, U. Trends in the Exchange Current for Hydrogen Evolution. *J. Electrochem. Soc.* **2005**, *152*, J23−J26.
(49) Tang, M. H.; Hahn, C.; Klobuchar, A. J.; Ng, J. W. D.; Wellendorff, J.; Bligaard, T.; Jaramillo, T. F. Nickel-silver alloy electrocatalysts for hydrogen evolution and oxidation in an alkaline electrolyte. *Phys. Chem. Chem. Phys.* **2014**, *16*, 19250−19257. , Publisher: The Royal Society of Chemistry
(50) Pluntke, Y.; Kibler, L. A.; Kolb, D. M. Unique activity of Pd monomers: hydrogen evolution at AuPd(111) surface alloys. *Phys. Chem. Chem. Phys.* **2008**, *10*, 3684−3688. , Publisher: The Royal Society of Chemistry
(51) Thomas, J. G. N. Kinetics of electrolytic hydrogen evolution and the adsorption of hydrogen by metals. *Trans. Faraday Soc.* **1961**, *57*, 1603−1611.
(52) Khanova, L. A.; Krishtalik, L. I. Kinetics of the hydrogen evolution reaction on gold electrode. A new case of the barrierless discharge. *J. Electroanal. Chem.* **2011**, *660*, 224−229.
(53) Kahyarian, A.; Brown, B.; Nesic, S. Mechanism of the Hydrogen Evolution Reaction in Mildly Acidic Environments on Gold. *J. Electrochem. Soc.* **2017**, *164*, H365−H374.
(54) Ives, D. J. G. Some Abnormal Hydrogen Electrode Reactions. *Can. J. Chem.* **1959**, *37*, 213−221.
(55) Bard, A. J.; Faulkner, L. R. *Electrochemical methods: fundamentals and applications;* 2nd ed.; Wiley: New York, 2001.
(56) He, Z.-D.; Chen, Y.-X.; Juarez, F.; Santos, E.; Schmickler, W. An Unusual Exchange Mechanism in the Tafel Reaction on Pt(110)-(1×1) Surfaces. *ChemElectroChem* **2019**, *6*, 3279−3284. , Publisher: John Wiley & Sons, Ltd
(57) Van den Bossche, M.; Skúlason, E.; Rose-Petruck, C.; Jónsson, H. Assessment of Constant-Potential Implicit Solvation Calculations of Electrochemical Energy Barriers for H_2 Evolution on Pt. *J. Phys. Chem. C* **2019**, *123*, 4116−4124. , Publisher: American Chemical Society
(58) Grabow, L. C.; Hvolbæk, B.; Nørskov, J. K. Understanding Trends in Catalytic Activity: The Effect of Adsorbate-Adsorbate Interactions for CO Oxidation Over Transition Metals. *Top. Catal.* **2010**, *53*, 298−310.
(59) Shi, C.; Hansen, H. A.; Lausche, A. C.; Nørskov, J. K. Trends in electrochemical CO2 reduction activity for open and close-packed metal surfaces. *Phys. Chem. Chem. Phys.* **2014**, *16*, 4720−4727.
(60) López-Cudero, A.; Cuesta, A.; Gutiérrez, C. Potential dependence of the saturation CO coverage of Pt electrodes: The origin of the pre-peak in CO-stripping voltammograms. Part 2: Pt(100). *J. Electroanal. Chem.* **2006**, *586*, 204−216.
(61) Norton, P. R.; Davies, J. A.; Jackman, T. E. Absolute coverages of CO and O on Pt(111); comparison of saturation CO coverages on Pt(100), (110) and (111) surfaces. *Surf. Sci. Lett.* **1982**, *122*, L593−L600.
(62) Protopopoff, E.; Marcus, P. Coadsorption of sulphur and hydrogen on Pt(111) studied by radiotracer and electrochemical techniques. *Surf. Sci. Lett.* **1986**, *169*, L237−L244.
(63) Protopopoff, E.; Marcus, P. Effects of chemisorbed sulphur on the hydrogen adsorption and evolution on metal single crystal surfaces. *J. Chim. Phys.* **1991**, *88*, 1423−1452. , Publisher: EDP Sciences
(64) Cave, E. R.; Shi, C.; Kuhl, K. P.; Hatsukade, T.; Abram, D. N.; Hahn, C.; Chan, K.; Jaramillo, T. F. Trends in the Catalytic Activity of Hydrogen Evolution during CO_2 Electroreduction on Transition Metals. *ACS Catal.* **2018**, *8*, 3035−3040.
(65) Zhang, Y.-J.; Sethuraman, V.; Michalsky, R.; Peterson, A. A. Competition between CO_2 Reduction and H_2 Evolution on Transition-Metal Electrocatalysts. *ACS Catal.* **2014**, *4*, 3742−3748.
(66) Varela, A. S.; Schlaup, C.; Jovanov, Z. P.; Malacrida, P.; Horch, S.; Stephens, I. E. L.; Chorkendorff, I. CO_2 Electroreduction on Well-Defined Bimetallic Surfaces: Cu Overlayers on Pt(111) and Pt(211). *J. Phys. Chem. C* **2013**, *117*, 20500−20508.
(67) Bandarenka, A. S.; Varela, A. S.; Karamad, M.; Calle-Vallejo, F.; Bech, L.; Perez-Alonso, F. J.; Rossmeisl, J.; Stephens, I. E. L.; Chorkendorff, I. Design of an Active Site towards Optimal Electrocatalysis: Overlayers, Surface Alloys and Near-Surface Alloys of Cu/Pt(111). *Angew. Chem., Int. Ed.* **2012**, *51*, 11845−11848.

■ NOTE ADDED AFTER ASAP PUBLICATION

This paper was published on the Web on December 15, 2020, without the author galley corrections made due to a production error. The corrected version was reposted on December 24, 2020.